

The potential role of electric fields and plasma barodiffusion on the inertial confinement fusion database

Peter Amendt, S. C. Wilks, C. Bellei, C. K. Li, and R. D. Petrasso

Citation: *Phys. Plasmas* **18**, 056308 (2011); doi: 10.1063/1.3577577

View online: <http://dx.doi.org/10.1063/1.3577577>

View Table of Contents: <http://pop.aip.org/resource/1/PHPAEN/v18/i5>

Published by the [American Institute of Physics](#).

Related Articles

Investigating inertial confinement fusion target fuel conditions through x-ray spectroscopy
[Phys. Plasmas](#) **19**, 056312 (2012)

Analytic criteria for shock ignition of fusion reactions in a central hot spot
[Phys. Plasmas](#) **18**, 102702 (2011)

Dynamic stabilization of Rayleigh–Taylor instability in an ablation front
[Phys. Plasmas](#) **18**, 012702 (2011)

The dependence of the virtual cathode in a Polywell™ on the coil current and background gas pressure
[Phys. Plasmas](#) **17**, 052510 (2010)

Rayleigh–Taylor instability in ion beam driven ablation fronts
[Phys. Plasmas](#) **16**, 082706 (2009)

Additional information on Phys. Plasmas

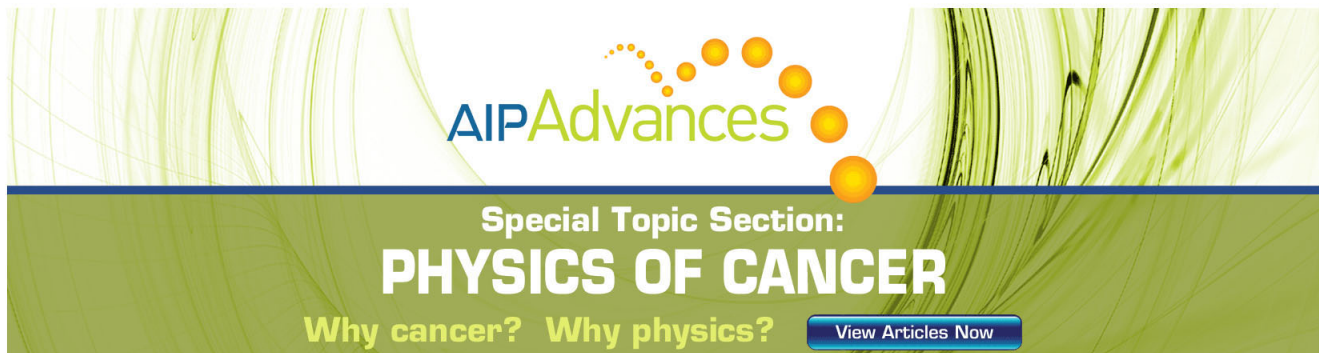
Journal Homepage: <http://pop.aip.org/>

Journal Information: http://pop.aip.org/about/about_the_journal

Top downloads: http://pop.aip.org/features/most_downloaded

Information for Authors: <http://pop.aip.org/authors>

ADVERTISEMENT



AIP Advances

Special Topic Section:
PHYSICS OF CANCER

Why cancer? Why physics? [View Articles Now](#)

The potential role of electric fields and plasma barodiffusion on the inertial confinement fusion database^{a)}

Peter Amendt,^{1,b)} S. C. Wilks,¹ C. Bellei,¹ C. K. Li,² and R. D. Petrasso²

¹Lawrence Livermore National Laboratory, Livermore, California 94551, USA.

²Plasma Science and Fusion Center, MIT, Cambridge, Massachusetts 02139, USA

(Received 30 November 2010; accepted 15 February 2011; published online 16 May 2011)

The generation of strong, self-generated electric fields (GV/m) in direct-drive, inertial-confinement-fusion (ICF) capsules has been reported [Rygg *et al.*, *Science* **319**, 1223 (2008); Li *et al.*, *Phys. Rev. Lett.* **100**, 225001 (2008)]. A candidate explanation for the origin of these fields based on charge separation across a plasma shock front was recently proposed [Amendt *et al.*, *Plasma Phys. Controlled Fusion* **51** 124048 (2009)]. The question arises whether such electric fields in imploding capsules can have observable consequences on target performance. Two well-known anomalies come to mind: (1) an observed $\approx 2\times$ greater-than-expected deficit of neutrons in an equimolar D³He fuel mixture compared with hydrodynamically equivalent D [Rygg *et al.*, *Phys. Plasmas* **13**, 052702 (2006)] and DT [Herrmann *et al.*, *Phys. Plasmas* **16**, 056312 (2009)] fuels, and (2) a similar shortfall of neutrons when trace amounts of argon are mixed with D in indirect-drive implosions [Lindl *et al.*, *Phys. Plasmas* **11**, 339 (2004)]. A new mechanism based on barodiffusion (or pressure gradient-driven diffusion) in a plasma is proposed that incorporates the presence of shock-generated electric fields to explain the reported anomalies. For implosions performed at the Omega laser facility [Boehly *et al.*, *Opt. Commun.* **133**, 495 (1997)], the (low Mach number) return shock has an appreciable scale length over which the lighter D ions can diffuse away from fuel center. The depletion of D fuel is estimated and found to lead to a corresponding reduction in neutrons, consistent with the anomalies observed in experiments for both argon-doped D fuels and D³He equimolar mixtures. The reverse diffusional flux of the heavier ions toward fuel center also increases the pressure from a concomitant increase in electron number density, resulting in lower stagnation pressures and larger imploded cores in agreement with gated, self-emission, x-ray imaging data. © 2011 American Institute of Physics. [doi:10.1063/1.3577577]

I. INTRODUCTION

The discovery of strong (\sim GV/m), self-generated electric fields in inertial-confinement-fusion (ICF) implosions using proton radiography¹ continues to generate interest in the implications of associated plasma phenomena for capsule performance.² The ICF implosion database is replete with anomalies that have defied explanations based on Euler fluid-based simulation tools. A notable example is the nearly $2\times$ deficit in observed-to-simulated neutron yields for an equal mixture (by ion number) of deuterium (D) and ³He compared with pure D fuels.³ Understanding this anomaly has direct implications for the goal of achieving high thermonuclear gain with D and tritium (T) fuels because the constituent ions have the same atomic weights as in D³He fuels. If an underlying plasma effect is responsible for the anomalously low yields, then the lower charge state of T (+1) relative to ³He (+2) may render an extrapolation to the behavior of DT fuels unfounded; otherwise, DT fuels could be expected to exhibit a similar degree of underperformance which would have adverse consequences for inertial fusion energy applications. Another example of anomalous yield

behavior in ICF implosions is the standard use of trace amounts of dopant to facilitate core imaging of x-ray self-emission near peak compression for an assessment of implosion compression and symmetry. Despite only 0.25 at. % concentration of argon in D, the observed yields suffer a 2–3 \times reduction.⁴

Another class of anomalous performance in ICF implosions is the tendency toward larger imploded core image sizes in fuel mixtures compared with predictions. In recent direct-drive experiments with DT and ³He mixtures, an image size $\sim 25\%$ larger than simulated was measured.⁵ For indirect-drive implosions on the Omega laser,⁶ a similar trend was seen when argon dopant was used: simulations predicted significantly smaller core images than what was observed.⁴ These observations showed less compression than expected and are qualitatively consistent with the measured deficit of neutrons. The question is what physical effect is responsible for these anomalies and whether it could potentially impact the behavior of IFE-relevant DT fuel mixtures.

Recently, a theory of plasma-based barodiffusion was advanced as a candidate explanation for the observed yield anomalies in fuel mixtures.⁷ Barodiffusion simply is pressure gradient-driven diffusion in contrast to the more familiar concentration gradient-driven diffusion. The idea of barodiffusion has been known for some time in the context of fluids

^{a)}Paper TI3 6, *Bull. Am. Phys. Soc.* **55**, 292 (2010).

^{b)}Invited speaker.

or gas dynamics,⁸ but its application to plasmas is only very recent.⁷ The notion of plasma-based barodiffusion arose from an attempt to understand the proton backlighting data of direct-drive ICF implosions on the Omega laser and the inferred strength of self-generated electric fields in the imploding fuel.¹ An interpretation of the data based on long length-scale electron pressure gradients for inferring the electric field strength fell short by 1 to 2 orders of magnitude, necessitating a consideration of other scenarios. An explanation was proposed that was based on the electric field generation at a shock front where an underlying charge separation occurs due to the high mobility of plasma electrons advancing slightly ahead of the ions in the shock front. The predicted behavior of these shock-driven electric fields matched well the measured transverse potential change of transiting (and deflected) 14.7 MeV protons ($\sim 10^5$ V) and was consistent with the measured abrupt sign change, arguably caused when the shock rebounds off the fuel center [in addition to the slightly later (100–200 ps) onset of deceleration of the fuel–pusher interface as described in Ref. 1]. The notion that the largest electric fields in an imploding fuel are localized to the shock front prompted speculation that other shock-front based phenomena could possibly play a role in explaining some of the outstanding anomalies in the ICF database. For example, barodiffusion across a shock front where the pressure gradients can be quite large, especially at high Mach numbers, is well known.⁹ However, the theory of barodiffusion with plasma electric fields and applied to an ICF implosion has not been considered until very recently.⁷ Depending on the circumstances at hand, an electric field can significantly affect the strength of barodiffusion. For the D^3He neutron anomaly,³ barodiffusion is increased in the presence of an electric field, whereas a mild decrease is predicted in the case of argon-doped D fuels. In the case of (DT) ignition experiments, the effects of shock-driven barodiffusion are predicted to not greatly affect performance since the cold and dense main fuel is well removed from the shock-heated region in the DT gas following shock rebound.

The physical picture of why barodiffusion may be large enough to matter in (subignition) ICF implosions is straightforward to describe. During an ICF implosion, strong pressure gradients (and electric fields) are produced at shock fronts. It is in these localized regions that barodiffusion can occur, in particular after shock coalescence at the origin. Indeed, as the incoming (high Mach number M) shock approaches the center of the fuel, the shock front is fairly narrow [$\sim O(1 \mu\text{m})$ or less] and species separation is expected to be strong but only very localized in space. As the shock rebounds from the origin, the shock is now much weaker ($M \cong 1$) but the front thickness is also considerably greater [$\sim O(100 \mu\text{m})$]. In this latter regime, barodiffusion can be shown to dominate over ordinary diffusion from concentration gradients but is reduced in strength.⁹ Within one or two shock front widths away from the origin, the spherically diverging geometry implies that a large volume for barodiffusion to operate over is now possible. If this volume is a significant fraction of the fuel volume (with typical radius ~ 100 to $200 \mu\text{m}$ in Omega-scale experiments), a significant shortfall of deuterium may result and lead to a neutron deficit, particularly since the cross section

for thermonuclear reactions is very temperature sensitive and the highest fuel temperatures occur near the center of the fuel. This net outward diffusion of the lighter ion species from the fuel center is possible since the ion mean-free-paths achieve by far their largest values during this stage of the implosion. Typically, ion temperatures reach several keV or more near the center of the fuel just after shock rebound (based on radiation–hydrodynamics simulations), and the ion mass density is on the order of 0.1 g/cc or less, resulting in ion mean-free-paths much in excess of a micron. The associated high degree of diffusion occurring after shock reversal is soon arrested by the increased fuel density and cooling of the center of the fuel from thermal conduction (until $-P \cdot dV$ work on the fuel takes over later on in the implosion). Thus, the episode of elevated ion diffusion following shock rebound may effectively establish the fuel composition and distribution for the succeeding phases of the implosion. Any deficit of ion species near the fuel center can be expected to persist throughout the implosion since the mean-free-paths quickly drop. For example, radiation–hydrodynamics simulations of hot-spot ignition capsules show ion mean-free-paths that reach several hundred microns at shock “flash” (or time when the first shock reaches the origin), only to fall to less than $10 \mu\text{m}$ within ~ 100 ps. By conservation of mass diffusional flux,⁹ the outward migration of the lighter ion species, e.g., D, must be compensated by a return flux of heavier ion species. The more massive ion species, e.g., 3He , carries more charge and more electrons because of the requirement of (nearly) strict charge neutrality. With the increased density of electrons near fuel center, the total pressure locally increases near deceleration onset. If an adiabatic implosion is assumed, a close correspondence between a greater fuel pressure near the onset of deceleration and a subsequent lower stagnation pressure is found. A lower stagnation pressure leads directly to a larger stagnation radius, in agreement with the observed trends for fuel mixtures. Note that the outward diffusing lighter ion species carries fewer electrons and effectively lowers the pressure away from the origin, yielding at first glance a compensating balance to the effects of the inwardly diffusing heavier species. However, the outward diffusing light ion species undergoes a strong geometrical dilution due to the spherical geometry, effectively reducing the compensating effects from the outwardly diffusing light ion species.

The key ingredient for shock-driven barodiffusion to play an important role in an ICF implosion is the scale of the shock-front thickness. The conventional (fluid-based) understanding is that a shock-front thickness should be on the order of an ion–ion mean-free-path λ_{ii} , which is typically less than a micron. However, a low Mach number plasma shock has been found to significantly deviate from this picture, according to early work by Jaffrin and Probst¹⁰ analyzing the Navier–Stokes equation (with electric fields) and later confirmed by Casanova *et al.* in their Fokker–Planck-based treatment.¹¹ At very small Mach numbers (< 1.12), electron thermal conduction and electron–ion energy exchange are the dominant dissipative mechanisms, and the ion-shock feature is coincident with the electron thermal shock with thickness of order $\sqrt{m_i/m_e} \times \lambda_{ii} \gg \lambda_{ii}$. At larger Mach numbers (~ 2) a distinct ion-shock feature arises

within the electron thermal shock, but the scale length for the ion feature has been found to still be considerably larger than λ_{ii} , i.e., nearly $20\times$. At still larger Mach numbers, but well outside the values of interest for a rebounding shock in an ICF implosion, the ion-shock-front thickness approaches λ_{ii} as expected. The main point is that the low Mach number return shocks (<1.5) of interest in an Omega implosion may have a characteristic front thickness larger than an ion–ion mean-free-path by as much as $20 - 100\times$, thereby potentially rendering a considerable volume within the fuel to a modest depletion of the lighter ion species from the effects of barodiffusion. Again, the two central ingredients for this scenario to operate in an ICF implosion are the spherically converging geometry of a capsule, enabling a shock front to encompass sufficient fuel volume, and the large shock-front thicknesses at low Mach number that may be on the order of a fuel radius following shock rebound.

The techniques of choice for studying the effects of barodiffusion on ICF performance beyond analytical arguments are somewhat limited. Standard Euler-based simulation techniques¹² are essentially a single-fluid description and cannot be expected to capture many or all of the salient multispecies effects as well as nonlocal kinetic effects. For example, shock fronts are not typically resolved in radiation–hydrodynamics simulations, and an artificial viscosity is implemented to legislate shock heating of the ions and to provide numerical stability against spurious acoustic signals. Molecular dynamics simulations could in principle model the physics of barodiffusion in detail, but they are limited in spatial scale ($<1 \mu\text{m}$) from practical considerations, particularly for low Mach number shocks. Fokker Planck simulations or techniques could bring to bear more understanding on this problem, but are computationally expensive, especially considering the disparate ion and electron time scales involved. Particle-in-cell (PIC) methods perhaps offer the most convenient path for assessing multispecies effects, particularly barodiffusion. The challenge with arriving at a comprehensive understanding of barodiffusion in ICF implosions is the need to include the highly transient nature of shock convergence at the origin and the evolution of the weak shock emanating from fuel center. The multispecies tools listed above have the potential capability to decisively address the true scope of shock formation and morphology in a transient, spherical geometry in place of the earlier analytical treatments that focused out of necessity on a planar geometry under steady-state conditions.¹⁰

In this paper we lay the groundwork for potentially explaining some of the key anomalies of the ICF database with fuel mixtures. In Sec. II we review the derivation of barodiffusion modeling with electric fields. Next we summarize in Sec. III the understanding of shock-front structure in a plasma and briefly look at the use of the hybrid code LSP (Ref. 13) to assess shock-front formation and structure in

multispecies plasmas. Section IV applies the theory to D^3He and D_2Ar fuel mixtures to help to explain the observed neutron anomalies. In Sec. V we apply the model to estimating the effect of barodiffusion on increased core image size. Section VI looks at topics for future work. We summarize and conclude in Sec. VII.

II. BARODIFFUSION THEORY

Pressure and temperature gradients generally lead to component separation in an initially homogeneous plasma. The associated mass diffusional flux of the lighter ion species is given by⁹

$$i_1 = -\rho D \left(\frac{d\alpha}{dx} + k_p \frac{d \ln P}{dx} + k_T \frac{d \ln T}{dx} \right) = -i_2, \quad (1)$$

where ρ is the total mass density, D is the diffusion coefficient, α is the light ion species (“1”) density fraction ρ_1/ρ , $k_p D$ is known as the barodiffusion coefficient, P is the total pressure, T is the (species ion and electron) temperature, k_T is the thermal diffusion ratio and i_2 is the mass diffusional flux of the heavier ion species (“2”). Equation (1) states that binary mass diffusion arises from gradients in concentration (classical diffusion), pressure (barodiffusion), and temperature (thermal diffusion). The barodiffusion ratio k_p can be determined by the thermodynamic (equilibrium) state of the mixture, while k_T is associated with an intrinsically nonthermodynamic local equilibrium state due to the heat flow. As such, k_T is a function of the ionic interactions and is directly amenable to a molecular dynamics simulation assessment. The assertion has been made that when the gradient scale lengths for pressure and temperature are comparable, barodiffusion is dominant.⁹ We ignore thermal diffusion in this work, though this assumption should be challenged through the use of molecular dynamics simulations or further analysis. We also ignore viscous contributions to Eq. (1), which should be an appropriate approximation in the case of weak (return) shocks that are the focus of this work. To obtain an expression for k_p we write for the local thermodynamic equilibrium ion distributions,

$$n_j \propto \exp \left(-\frac{m_j g x}{k_B T} - \frac{Z_j e \Phi}{k_B T} \right), \quad (2)$$

where m_j is the ion mass for species $j = 1, 2$, g is the underlying (uniform) acceleration, x is the one-dimensional position coordinate, k_B is Boltzmann’s constant, Z_j is the ion charge state of species j , $-e$ is the electron charge, Φ is the electrostatic potential, and both species are assumed to have a common (constant) temperature. Upon setting the diffusional mass flux to zero under steady-state equilibrium conditions $d\alpha/dx + k_p d \ln P/dx = 0$, and assuming ideal equations of state, we obtain

$$k_p = \frac{\alpha(1-\alpha)(m_2-m_1) \left[\frac{\alpha(1+Z_1)}{m_1} + \frac{(1-\alpha)(1+Z_2)}{m_2} \right] \cdot \left[1 - \frac{eE}{m_1 g} \cdot \frac{Z_2-Z_1}{m_2/m_1-1} \right]}{\alpha(1+Z_1) + (1-\alpha)(1+Z_2) - \frac{eE}{m_1 g} \left[\alpha Z_1(1+Z_1) + (1-\alpha)Z_2(1+Z_2) \cdot \frac{m_1}{m_2} \right]}, \quad (3)$$

where $E = -\nabla\Phi$ is the electric field. For unequal electron and ion temperatures, Eq. (3) is easily modified according to the prescription: $1 + Z_j \rightarrow 1 + Z_j \times T_e/T_i$, where T_e (T_i) is the electron (ion) temperature. Equation (3) reduces to the standard fluid result when $Z_1 = Z_2 = 0$, $E = 0$:⁹

$$k_p = \alpha(1 - \alpha)(m_2 - m_1) \left[\frac{\alpha}{m_1} + \frac{(1 - \alpha)}{m_2} \right]. \quad (4)$$

To proceed further for the plasma case, the ratio eE/m_1g must be evaluated. We consider two cases: (i) an isothermal, accelerating atmosphere with a large length-scale self-generated electric field satisfying $eE/m_1g = O(1)$ and (ii) $eE/m_1g \gg 1$ as in a plasma shock front.

For the case (i) of an isothermal, uniformly accelerating atmosphere in near steady state, e.g., an imploding capsule, the self-generated electric field follows from the Boltzmann relation after neglecting the electron inertia: $E = -\nabla P_e/en_e$, where P_e is the total electron pressure and n_e the electron density. Using Eq. (2) and ideal equations of state for the electrons, it readily follows that

$$\frac{eE}{m_1g} = \frac{\alpha Z_1 + (1 - \alpha)Z_2}{\alpha Z_1(1 + Z_1) + (1 - \alpha)Z_2(1 + Z_2)m_1/m_2}, \quad (5)$$

where gradients in Z_j are neglected. For the case of equal isotopes ($Z_1 = Z_2 \equiv Z$), Eqs. (3) and (5) reduce to

$$k_p = \alpha(1 - \alpha)(m_2 - m_1) \left(\frac{\alpha}{m_1} + \frac{1 - \alpha}{m_2} \right) (1 + Z). \quad (6)$$

For the hydrogen isotopes ($Z = 1$), plasma electric fields increase the strength of barodiffusion through k_p by $2\times$. In the case of $D^3\text{He}$, Eqs. (3) and (5) give a value for k_p that is identically zero, independent of light ion mass fraction (α).

For case (ii), we evaluate Eq. (3) in the limit $eE/m_1g \gg 1$ as pertaining to a plasma shock front, obtaining

$$k_p = \alpha(1 - \alpha) \times (Z_2 - Z_1) \left[\frac{\alpha(1 + Z_1) + (1 - \alpha)(1 + Z_2)m_1/m_2}{\alpha Z_1(1 + Z_1) + (1 - \alpha)Z_2(1 + Z_2)m_1/m_2} \right]. \quad (7)$$

This limit is distinguished from the fluid case (Eq. (4)) by a strong dependence on the difference in species ionization states instead of component masses. Such a feature has possible implications for the behavior of DT fuel mixtures compared with $D^3\text{He}$: a fluid explanation of the $D^3\text{He}$ neutron anomaly based on Eq. (4) would predict a similar degradation for an equimolar DT mixture, whereas Eq. (7) for a shocked plasma would claim otherwise. Note also that k_p depends more strongly on the difference in ionization states, as opposed to the difference in charge-to-mass ratio for each species. The reason for this dependence is that the pressure gradients are also important,¹⁰ particularly across a shock front, whereby a simple Z_j/m_j scaling argument based only on the dynamics of charged particles does not provide a complete representation.

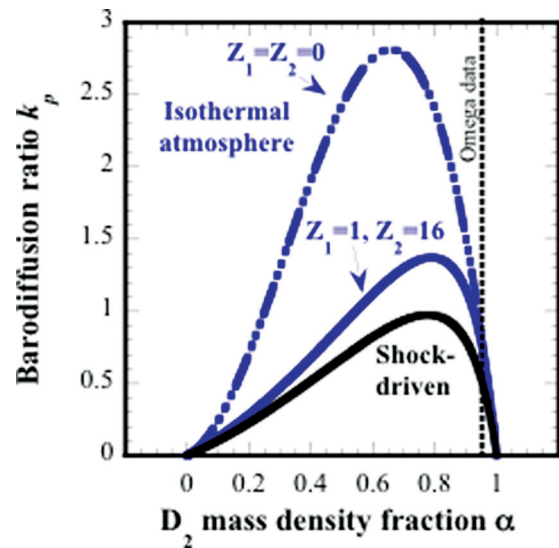


FIG. 1. (Color) Barodiffusion ratio k_p vs deuterium mass density fraction α in He-like argon mixture for isothermal atmosphere (blue) and shock-driven cases (black) with gas-dynamical limit ($Z_1 = Z_2 = 0$) shown as dotted-dashed line; vertical dashed line represents Omega data with $\alpha = 0.95$.

Figure 1 compares the strength of the barodiffusion ratio k_p between an isothermal atmosphere and a plasma shock for a deuterium fuel doped with varying amounts of (He-like) argon. For α not too close to unity, the former case is nearly 30% stronger than the shock-driven case, and the fluid limit ($Z_j = 0$) shows a nearly $2\times$ greater enhancement over the plasma analog in this particular example. However, the strength of barodiffusion between these two cases can differ significantly, depending on the stage of the implosion where each effect has maximum effect. In the case of an isothermal atmosphere, the pressure-gradient scale length varies as C_s^2/g , reaching a minimum value ($\cong 10 \mu\text{m}$) after deceleration onset when g is greatest. For a shocked fuel, the maximum effect is achieved before deceleration onset immediately following shock rebound from the fuel center. At this stage of the implosion, the ion mean-free-paths are a significant fraction of the fuel radius, and barodiffusion across the shock front can give rise to significant light ion loss from the center provided the shock-front thickness is appreciably large.

III. PLASMA SHOCKS

A. Summary of Jaffrin and Probstein analysis

The strength of barodiffusion across a shock front in an ICF implosion critically depends on the thickness of the shock front. As the strong, incoming shock rebounds from the fuel center, the outgoing return shock is necessarily much weaker with a corresponding increase in width compared with a (postshock) ion-ion mean free path λ_{ii} . The notion of a shock having a width on the order of λ_{ii} is based on gas-dynamics studies of shocks at high Mach number. However, the state of the fuel following shock rebound is often a fully ionized plasma in contrast to a classical fluid. Particularly at low Mach number, the structure of a plasma shock can differ markedly from a fluid shock. Jaffrin and

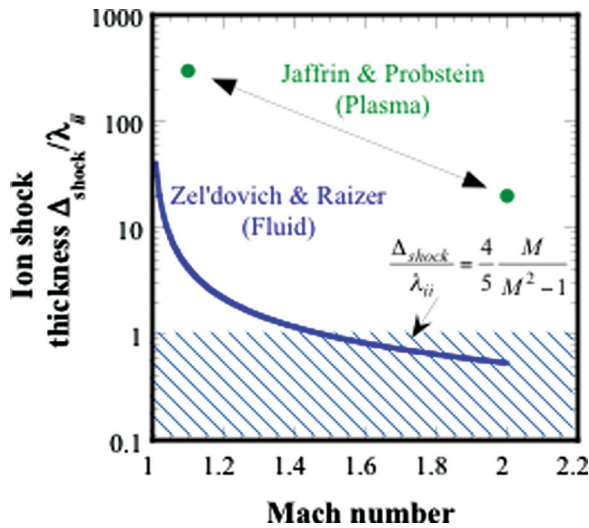


FIG. 2. (Color) Ion-shock thickness normalized to ion-ion mean free path vs Mach number according to gas-dynamical treatment with $\gamma = 5/3$ (blue) and multicomponent plasma analysis (green).

Probst¹⁰ performed a detailed, steady-state, one-dimensional analysis of the Navier–Stokes equations for both ions and electrons, including Gauss’ law for the self-generated electric fields, and the energy and mass conservation equations.¹⁰ Several examples were considered, beginning with the low Mach number case $M = 1.12$. A broad shock solution was found where both the ion and electron structures had spatial scales on the order of $\lambda_{ie} \equiv \lambda_{ii} \sqrt{m_i/m_e} \gg \lambda_{ii}$, where m_e (m_i) is the electron (ion) mass. In this case, ion viscosity is small compared to the dissipative mechanisms of electron thermal conduction and electron–ion energy exchange, where the latter effects are identified with the characteristic λ_{ie} length scales. Next, the $M = 2$ case was studied where a distinct ion-shock feature was found to emerge within a broader electron thermal shock layer of thickness λ_{ie} . The width of the ion feature was found to be considerably larger than an ion mean-free-path by nearly a factor-of-20. A final example for $M = 10$ was also studied where a distinct electron preshock thermal layer was seen a distance λ_{ie} ahead of the ion-shock feature. Figure 2 compares the predictions of this plasma shock analysis at low Mach number with a gas-dynamical scaling for the thickness of the ion-shock feature with ratio of specific heats $\gamma = 5/3$. A

nearly 100-fold increase in (ion) shock-front thickness over gas-dynamics predictions is seen for $M < 1.5$, the representative range of Mach numbers for the rebounding shock in ICF implosions. According to this analysis, the return shock front thickness may well be on the order of a fuel radius, although time-dependent effects and the spherical geometry of an ICF implosion could significantly affect this assertion.

B. LSP hybrid PIC simulations

Multispecies, (ion) kinetic simulations with the hybrid, collisional PIC code LSP (Ref. 13) tend to confirm the original analysis of Jaffrin and Probst. Figure 3(a) shows the simulated shock structure at $M = 1.25$ with an ion-shock feature that is virtually indistinguishable from an electron thermal shock feature (not shown). The ions were modeled as fully kinetic PIC particles in LSP to provide the physical viscosity, while the electrons were modeled as fluid (macro) particles having a characteristic (local) temperature. The self-generated electric fields were found using an alternating direction implicit solver in LSP. In order to confirm the integrity of a plasma shock with LSP, a classic shock-tube problem¹⁴ (in the laboratory frame) was run with the electric field switched off in order to verify that the ion viscosity produces the correct shock behavior in this configuration. This procedure also eliminates the need for an artificial viscosity, which is typically required when modeling shocks in standard, Euler-based radiation–hydrodynamics codes. This means that the electron fluid (macro) particles are assigned a position and velocity, but they also have an internal energy. Thus, the particles are moved according to an ensemble velocity, with a pressure-gradient term added to the equation of motion. Each particle carries an internal energy that consists of $-P \cdot dV$ work, thermalization between species, heat conduction, Ohmic losses, and inelastic losses between electrons and ions. For computational efficiency and owing to the small electron–electron mean-free-paths ($\ll 1 \mu\text{m}$), kinetic effects for the electrons are not included in such a model at present, but further work will aim to relax this constraint.

Care must be taken to set up the system such that a steady-state shock will be set up shortly after $t = 0$. This requires choosing the (equal) electron and ion velocities behind the shock correctly, given a particular set of (equal) ion and electron temperatures and densities on both sides of

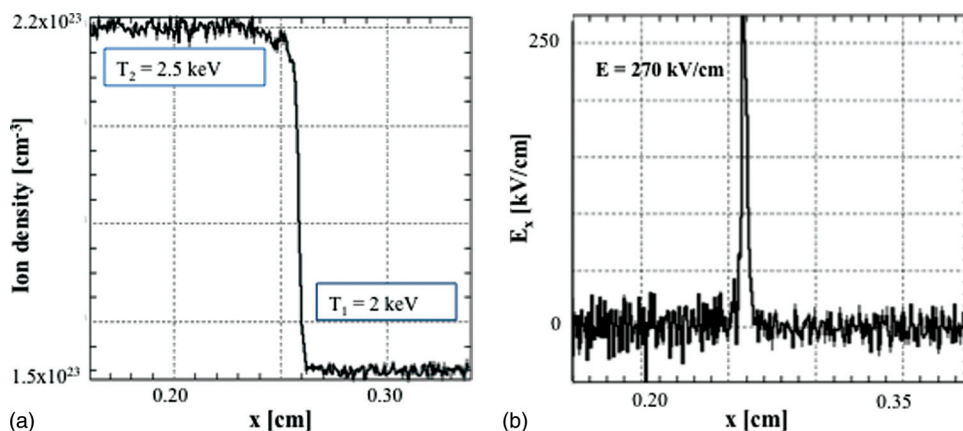


FIG. 3. (Color online) Ion number density profile (a) and associated, self-generated electric field (b) for $M = 1.25$ planar shock in deuterium according to LSP simulation using kinetic ions and fluid electrons. Indicated temperatures are chosen initial electron and ion temperatures ahead of (T_0) and behind (T_1) shock front as constrained by Hugoniot relations for $\gamma = 5/3$ gas.

the shock for a chosen Mach number and consistent with the Hugoniot relations. As mentioned above, the shock front thickness can be many ion mean-free-paths wide, in contrast to the usually assumed ion–ion mean-free-path that most radiation–hydrodynamics codes implicitly assume. In the case shown in Fig. 3(a), we observe a front thickness of nearly 100 μm , which is much larger than a Debye length [$\sim O(1 \text{ nm})$]. This is close to what is expected from the analysis of Jaffrin and Probst and greater than an ion–ion mean-free-path by almost a factor-of-100. An associated self-generated electric field with strength of nearly 270 kV/cm is also indicated from Fig. 3(b), which is close to analytical estimates as well as the inferred experimental value immediately following shock rebound.¹ The physical source of the simulated electric field is the gradient in electron pressure which leads to a slightly ion rich (lean) region to the left (right) of the E_x -field maximum. The simulated potential change across the shock front is about 2 kV, in agreement with analytical estimates ($\approx k_B T_e/e$). Although this specific example holds some interest on its own, the important result here is that we now have demonstrated the capability to study ion behavior in a shock when realistic shock fronts, electric fields, and kinetic effects are all taken into account.

C. Barodiffusion strength at low Mach number

In the low Mach number regime, it can be shown that barodiffusion dominates over classical diffusion. For a weak shock we write $\Delta P = P_1 - P_0$ as a first order quantity, where P_1 (P_0) is the postshock (pre-shock) pressure. The concentration-gradient contribution in Eq. (1) can be shown to be proportional to $(\Delta P)^3$, while the pressure-gradient contribution is of order $(\Delta P)^2$.⁹ As $\Delta P = 2\gamma P_1(M^2 - 1)/M(\gamma + 1) \propto M - 1$ at low Mach number, the barodiffusion scaling is $(M - 1)^{-1}$ stronger than the classical diffusion source term.

The mass diffusional flux due to barodiffusion alone readily follows from Eq. (1): $i_1 = \rho C_s k_p (\Delta P/P)^2$ for a gas-dynamical shock, or for the case of a plasma shock $i_1 = 2\rho C_s k_p (\Delta P/P)/\eta$, where $C_s \approx D/\lambda_{ii}$ is the sound speed and η is the ratio of (ion) front thickness in a plasma shock to a gas-dynamical shock (cf., Fig. 2). The factor-of-2 enhancement for the plasma shock case is ascribed to ambipolar diffusion for an equal (ion and electron) temperature, hydrogen plasma. Operationally, the two descriptions are similar at small Mach number, but we choose to proceed further with the gas-dynamical description of the shock that conveniently relates ΔP to the Mach number. The amount of barodiffused light ion species scales as $i_1 \times 4\pi\Delta_{\text{shock}}^2\tau$, where τ is the (return) shock-transit time over a shock width Δ_{shock} . Consequently, the fraction of diffused deuterium $\Delta M_1/M_1$ over the enclosed fuel mass M_1 is estimated as⁷

$$\frac{\Delta M_1}{M_1} \cong \frac{3k_p}{\alpha M^3} \frac{4\gamma^2(M^2 - 1)^2}{(\gamma + 1)^2}. \quad (8)$$

An important feature of Eq. (8) to note is the leading order cancellation of α since $k_p \propto \alpha$ (cf., Eq. (3)). Thus, the fraction of diffused light ion mass approaches a constant value

as $\alpha \rightarrow 0$ in the absence of mitigating physical effects. Two physical effects are identified that may offset this trend. First, the average sound speed increases inversely with α due to the increasing charge-to-mass ratio

$$C_s(f) = C_s(1) \sqrt{\alpha + \frac{Z_2 m_2}{Z_1 m_1} (1 - \alpha)} = C_s(1) \sqrt{\frac{f + \frac{Z_2}{Z_1} (1 - f)}{f + \frac{m_2}{m_1} (1 - f)}}, \quad (9)$$

where $f \equiv n_1/(n_1 + n_2)$ is the light ion number density fraction. Radiation–hydrodynamics simulations suggest that the speed of the shock in an ICF implosion mildly increases with α , implying overall that the Mach number increases with α . A possible physical explanation is that for a low Mach number shock with its associated large front thickness, radiative cooling from the more abundant higher- Z , heavier ion species at small values of f leads to a reduced ion temperature and Mach number (which, to a good approximation, equals the ratio of the post- to pre-shock ion temperature for $M < 2$). A second, potentially more important effect is the increased collisionality of the lighter ion species with the heavier species at small α . At higher concentrations of the heavier ions, the increased collisionality $[fZ_1 + (1 - f)Z_2]^2/Z_1^2$ helps to reduce the outward diffusion of the light ion species away from fuel center, significantly reducing the effects of barodiffusion for small values of f . The diffusion scale length for the lighter ion species $\sqrt{D\tau}$ scales as

$$\sqrt{D\tau} = \Delta_{\text{shock}} \sqrt{\frac{C_s(f)}{M(f)v_{T1}(f)} \cdot \frac{\lambda_{12}(f)}{\Delta_{\text{shock}}}}, \quad (10)$$

where $\lambda_{12} = v_{T1}/v_{12}$ is the mean-free-path of a light ion in a background of heavy ions (species “2”), $v_{T1} = \sqrt{k_B T/m_1}$ is the light ion thermal speed, and

$$v_{12}(f) = v_{11}(f)(1 - f) \left(\frac{Z_2}{Z_1}\right)^2 \frac{1 + Z_1}{f(1 + Z_1) + (1 - f)(1 + Z_2)} \times \sqrt{\frac{2m_2}{m_1 + m_2}} \quad (11a)$$

is the Spitzer collision rate between species “1” and “2” written as a function of the self-collision rate for species “1,”

$$v_{11}(f) = \frac{v_{11}(1)f(1 + Z_1)}{f(1 + Z_1) + (1 - f)(1 + Z_2)}. \quad (11b)$$

According to radiation–hydrodynamic simulations of weak shocks that are computationally resolvable, the width of the shock front is not a strong function of the average ionization state of the plasma. In contrast, the average ion mean-free-path strongly scales as $1/Z^4$, giving nearly a factor-of-16 difference in expected shock width between a pure ^3He and D_2 plasma. Again, radiative cooling across the shock front could be responsible for this difference (see Sec. IV A).

An additional physical mechanism that increases the strength of the diffusion coefficient in the presence of a self-generated electric field across the plasma shock front can be

identified. The change in forward velocity of a light ion over a collision time in the presence of a parallel electric field obeys

$$\Delta v = \frac{Z_1 e E}{m_1} \cdot \tau_{12} \cong \frac{Z_1 e}{m_1} \frac{k_B T_e}{e \Delta_{\text{shock}}} \frac{\lambda_{12}}{v_{T1}} = \frac{C_{s1}^2}{v_{T1}} \frac{\lambda_{12}}{\Delta_{\text{shock}}}, \quad (12)$$

where C_{s1} is the sound speed for species “1” ($f = 1$). On the other hand, $D_0 \approx C_s^2(f) \tau_{12} \rightarrow D_0 \cdot (1 + \Delta v/v_{T1})^3 = D_0(1 + Z_1 \lambda_{12}/\Delta_{\text{shock}})^3$, where D_0 is the classical diffusion coefficient in the absence of an electric field and the energy scaling of collision frequency $\propto E^{-3/2}$ is used. If $\lambda_{12}/\Delta_{\text{shock}} = O(1)$ for example, then for $Z = 1$ the classical diffusion coefficient may be enhanced by nearly an order-of-magnitude.

The strength of shock-driven barodiffusion rests on the degree to which ions can diffuse across a significant fraction of a shock-front width during shock transit. The amount of barodiffused light ions thus scales as follows:

$$\frac{\Delta M_1}{M_1} \rightarrow \frac{\Delta M_1}{M_1} \cdot \left(\frac{D(f) \tau_{12}(f)}{D(1) \tau_{12}(1)} \right)^{3/2}. \quad (13)$$

To estimate the fraction of a shock front diffused in an arbitrary fuel mixture, we rewrite Eq. (10) as

$$\sqrt{D \tau_{12}} = \Delta_{\text{shock}} \sqrt{\frac{M^2 - 1}{\eta M^2 \gamma^{1/2}}} \cdot [f + (1-f)Z_2/Z_1]^{3/4} \times \left[1 + \frac{\gamma(M^2 - 1)[f + (1-f)Z_2/Z_1]^2}{\eta} \right]^{3/2}, \quad (14)$$

where $\lambda_{12}/\Delta_{\text{shock}} \approx [Z_1/\bar{Z}(f)]^2 \eta M/(M^2 - 1)$, $\bar{Z} = fZ_1 + (1-f)Z_2$ is an average ionization state of the fuel, the last term in square brackets represents the enhancement in diffusion from a self-generated electric field, and η is the ratio of plasma shock width to fluid shock width. If $\gamma = 5/3$, $M = 1.5$, $f = 0$, and $\eta = 20$ are chosen as an example for a $D^3\text{He}$ mixture, the diffusion length is an appreciable \sim one-third of a shock-front width. For the effects of barodiffusion to occur in an ICF implosion, it is not necessary that the diffusion length match a shock-front thickness, but only that the diffusion length approximately coincide with the high temperature region responsible for the majority of thermonuclear reactions—30%–50% of the fuel radius. With an ion–ion mean-free-path of several microns or more following shock flash near fuel center and $\eta \cong 20 - 100$, this condition is typically met.

IV. NEUTRON YIELD ANOMALIES

Section III described the formalism for estimating the influence of shock-induced barodiffusion on depleting the region near the fuel center of the lighter ion species in a fuel mixture, e.g., deuterium. Equations (8), (13), and (14) provide an estimate on the fraction of depleted fuel by mass. As the thermonuclear cross section is proportional to the product of the densities, the degree of neutron yield degradation can be straightforwardly estimated. We consider two outstanding examples in the Omega database that may be explained by the barodiffusion effect.

A. $D^3\text{He}$ implosions

A significant ($\approx 2\times$) neutron deficit in “hydrodynamically equivalent” $D^3\text{He}$ fuel mixtures with direct drive on the Omega laser facility has been reported.³ A sequence of implosions was performed where the various fuel mixtures preserved mass and number density in order to maintain fixed conditions for hydrodynamic instability growth and fuel convergence. For a 50-50 mixture of deuterium and ^3He by ion number, an anomalous factor-of-2 reduction in DD neutrons (2.45 MeV) compared with predictions and relative to nearly pure D_2 and ^3He fuels was observed.

Figure 4 shows the hydrodynamically equivalent implosion data³ for two capsule shell thicknesses and overlaid with the model for two choices of average return-shock Mach number that are based on radiation–hydrodynamics simulations. The model trend tracks the data fairly well, although a modest offset in the model toward higher values of deuterium concentration is apparent. Much of this shift may be due to the ion diffusion model used, and the lack of allowance for radiative cooling (leading to reduced Mach number) as the concentration of the heavier ion species increases, i.e., decreasing f . With the broad shock fronts of interest here, the shock-transit times are on the order of 100 ps, which allows ample time for radiative cooling.

In applying the barodiffusion model, we have assumed that the temperature of both ion species is unchanged with fuel mixture. As the thermonuclear cross section is a strong function of temperature, any possible deviation from the constant temperature assumption could significantly affect the neutron yields as α varies. We can check this assumption by using the constraints imposed by hydrodynamical equivalence: constant total pressure and mass density for all fuel mixtures, to find

$$T(f) = \left[f + (1-f) \frac{m_2}{m_1} \right] \frac{T(1)(1+Z_1)}{f(1+Z_1) + (1-f)(1+Z_2)},$$

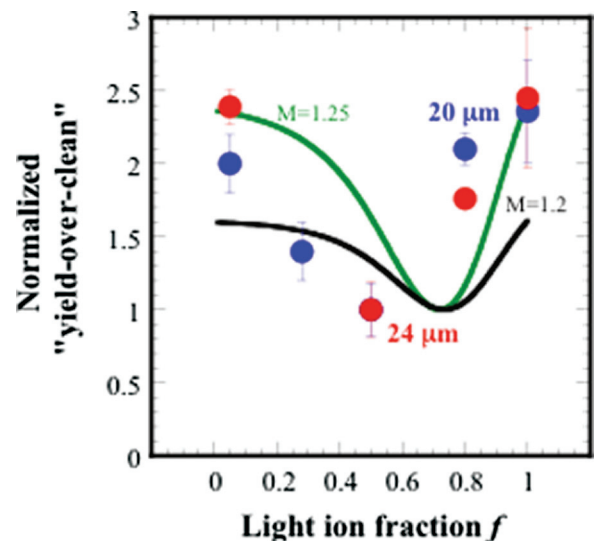


FIG. 4. (Color) Ratio of measured-to-simulated DD neutron yields normalized to 50-50 $D^3\text{He}$ fuel mixture for initial 20 (blue) and 24 (μm) thick, hydrodynamically equivalent, directly driven plastic (CH) capsules with overlaid barodiffusion model curves for Mach numbers $M = 1.25$ (green) and $M = 1.2$ (black).

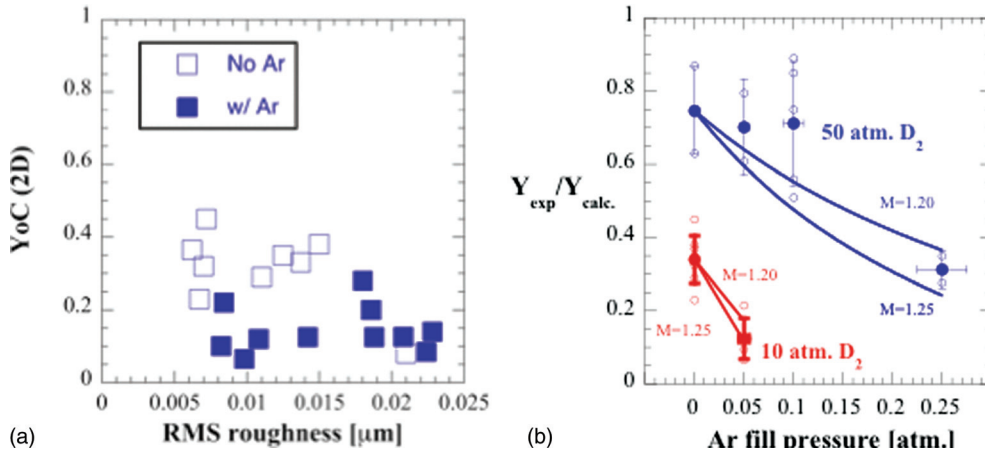


FIG. 5. (Color) (a) Ratio of measured-to-simulated DD neutron yields without an allowance for fuel–pusher mix (“clean”) vs root-mean-squared surface roughness; (b) ratio of measured-to-simulated (clean) DD neutron yields vs argon fill pressure for 50 atm DD fill (blue) and 10 atm fill (red) in plastic capsules. Solid symbols denote averages over individual shots shown as open circles; 10 atm data as shown are limited to nominally smooth surface finishes with root-mean-square amplitudes ≤ 15 nm. Solid curves denote barodiffusion model for indicated Mach numbers M and average ionization state of argon $Z_2 = 16$.

where T is the ion or electron temperature. As long as $(1 + Z_2)/(1 + Z_1) = m_2/m_1$ is satisfied, T remains constant for all fuel mixtures—as is the case for D^3He fuel mixtures. Again, the underlying assumption of isothermal conditions, i.e., spatially uniform temperature, may have a significant impact on interpreting the data beyond the barodiffusion hypothesis, which is the subject of ongoing research.

B. D_2Ar implosions

The indirect-drive implosion database on the Omega laser facility has made frequent use of mid- Z dopants in the deuterium fuel to increase x-ray self-emission near peak compression. Interestingly, a systematic 2–3 \times decrease in DD neutron yields was consistently observed despite only 0.25 at. % argon dopant levels.⁴ Figure 5(a) shows the ratio of observed yield to predicted yield with two-dimensional radiation–hydrodynamics simulations versus root-mean-squared surface roughness of plastic capsules (doped with 1.0 at. % germanium) and filled with 10 atm of deuterium fuel.

Figure 5(b) shows the barodiffusion modeling applied to this 10 atm fuel fill dataset as well as a 50 atm DD database for several argon dopant levels. The model is normalized to the nondopant case for each DD fill pressure, and the data are well bracketed by the two choices of Mach number as shown. A challenge with implementing the model as described herein is the reliance on radiation–hydrodynamics simulations for obtaining critical information on the outgoing return (plasma) shock. How close these simulations succeed in reproducing the properties of plasma shocks at low Mach number awaits confirmation by PIC simulation techniques (see Sec. III B). In addition, the transient nature of the outgoing shock following rebound from target center presents a challenge in defining a representative Mach number value for input to the simple barodiffusion model. Despite these operational caveats, the barodiffusion model succeeds in tracking the observed trend in neutron yield degradation with argon dopant levels for these two fuel pressure fills.

V. IMAGE-SIZE ANOMALIES

The outward diffusion of the deuterium from barodiffusion must be balanced by an inward mass flux of heavier

ion species. The heavier ions, e.g., 3He or Ar, carry more electrons toward the fuel center owing to the requirement of charge neutrality. The extra electrons contribute to the total pressure, and result in a local surplus of pressure near fuel center. The outward flux of lighter ions results in less pressure away from fuel center, but this potential cooling effect is geometrically diluted by spherical divergence. The locally higher pressure near fuel center after shock rebound is presumed to persist to the instant of deceleration onset, typically 100–200 ps later, based on causality constraints imposed by an acoustic transit time across the fuel. Assuming that the implosion evolves adiabatically, the greater fuel pressure at deceleration onset can be directly related to a lower stagnation pressure, resulting in lower fuel convergence and larger self-emission core images as reported for D^3He and D_2Ar fuel mixtures.

To develop the model, we start with mass flux conservation in spherical geometry,

$$v_1[\rho'_1 - \rho_1](1 + \varepsilon)^2 = -v_2[\rho'_2 - \rho_2](1 - \varepsilon)^2, \quad (15)$$

where v_j is the speed of the j th ion species, primed (unprimed) quantities denote the state of the ion species with (without) barodiffusion, and ε represents the fraction of a shock width that the light (heavy) ions have diffused ahead of (behind) the shock. Assuming equal temperatures for both ion species, an expression for the ratio of (total) pressures for the heavier ion species with and without barodiffusion follows straightforwardly,

$$\begin{aligned} \frac{P'}{P} &= \frac{(Z_1 + 1)n'_1 + (Z_2 + 1)n'_2}{(Z_1 + 1)n_1 + (Z_2 + 1)n_2} \\ &= \frac{1 + \Delta M_1/M_1}{(Z_1 + 1)f + (Z_2 + 1)(1 - f)} \\ &\quad \times \left[(Z_1 + 1)f + (Z_2 + 1) \frac{(1 - f)}{1 + \Delta M_1/M_1} \right. \\ &\quad \left. \times \left(1 - \frac{\Delta M_1}{M_1} \cdot \frac{f}{1 - f} \cdot \sqrt{\frac{m_1}{m_2}} \left(\frac{1 + \varepsilon}{1 - \varepsilon} \right)^2 \right) \right] > 1. \quad (16) \end{aligned}$$

Next, we relate the stagnation pressure P_{stag} to the pressure at deceleration onset P_d for an adiabatic implosion ($\gamma = 5/3$), after invoking energy conservation,

$$P_{\text{stag}} = P_d \left(\frac{m_p v_d^2 / 2}{4\pi r_d^3 P_d / 3} \right)^{5/2}, \quad (17)$$

where m_p is the mass of the ablating shell or pusher, v_d is the (peak) implosion speed of the pusher at deceleration onset, r_d is the radius of the fuel at deceleration onset, and $(r_{\text{stag}}/r_d)^2 \ll 1$ is assumed. The stagnation radius, in turn, is related to P_d as follows: $r_{\text{stag}} = r_d \cdot (P_d/P_{\text{stag}})^{1/5}$. Thus, a candidate physical process (such as barodiffusion) that leads to increased central fuel pressure at deceleration onset could lead to reduced stagnation pressure and increased stagnation radius. The potential neutralizing influence of the outward barodiffusion of lighter ions and their associated lower pressure is much reduced ($\cong 7\times$) by the spherical divergence of the return shock after a shock transit over a front thickness.

A. (DT)³He

An example of an oversized x-ray core image compared with simulations was reported by Herrmann *et al.*, using a fuel mixture of DT and ³He ($f = 0.6$) in direct drive.⁵ A nearly 25% larger image size (in radius) was inferred compared with predictions. We now apply Eqs. (16) and (17) to assess how large a barodiffusion-based effect could be. Figure 6 shows the ratio of stagnation radius with and without barodiffusion versus light ion mass fraction α for three choices of return-shock Mach number. The spherical geometry factor ε is taken as $1/2$ to represent on average the outward (inward) migration of light (heavy) ions by half a shock width when the center of the return shock front as moved one entire shock width distance from the origin. According to Fig. 6, the stagnation radius is 20%–40% larger for this range of Mach numbers due to the effects of barodiffusion. However, there is the potential that

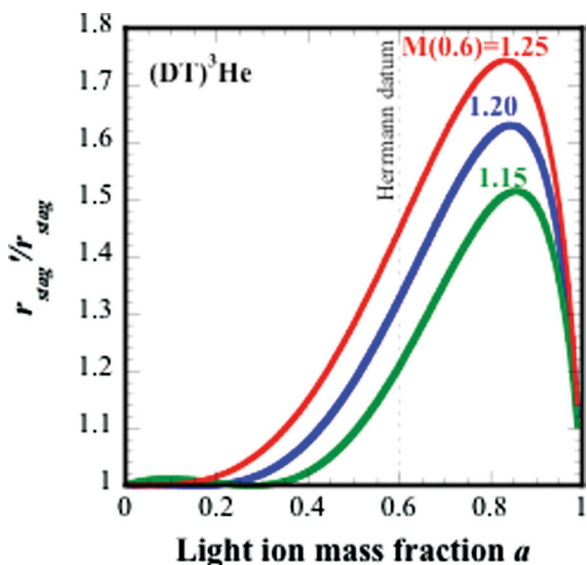


FIG. 6. (Color) Ratio of fuel stagnation radius with and without barodiffusion model vs light ion mass fraction in (DT)³He fuel mixture for three Mach numbers; Herrmann *et al.* datum is shown as dotted line ($\alpha = 0.6$).

the x-ray image contours used to infer an imploded fuel convergence could be skewed by the greater abundance of the heavier ion species near fuel center. For example, the associated greater emissivity in x-rays near the origin could affect the measured self-emission contours in the form of an apparent contraction, thereby possibly negating the barodiffusive effect on image size. We can estimate this effect as follows. For the case of a (DT)³He mixture, thermal Bremsstrahlung emission dominates: $W_{\text{IB}} \approx \sqrt{T} Z^2 n_e n_i = \sqrt{T} Z^2 P_{\text{stag}}^2 / (Z+1)^2 T^2 \approx Z^3 / (Z+1)^2 T^{3/2} P_d^3$. For an adiabatic fuel compression, $T \approx n_2^{2/3} \approx r_{\text{stag}}^{-2} \approx 1/P_d \Rightarrow W_{\text{IB}} \approx Z^3 / (Z+1)^2 P_d^{3/2}$. For a 50% increase in P_d and $Z \rightarrow 2$ as an upper bound if the fuel center is populated entirely with ³He, W_{IB} increases by only 10%. This modest enhancement in self-emission leads to only a $\sim 5\%$ correction for the 50% (assumed) Gaussian x-ray contour. Thus, a potential redistribution of self-emission from excessive ³He abundance at fuel center affects little the inferred change in size of the fuel due to barodiffusion.

B. D₂Ar

Another example of enhanced x-ray image size in ICF implosions is the use of trace amounts of argon to enhance core self-emission for diagnosing imploded fuel conditions. The data consistently show an insensitivity of image size to dopant level, contrary to radiation–hydrodynamics simulation predictions of a nearly 30% reduction in image size. The hohlraum-driven capsules are 1.0 at. % Ge-doped CH shells containing 10 atm of deuterium. The argon dopant levels used were 0.05 atm. Figure 7 shows the ratio of stagnation radius with and without barodiffusion versus light mass fraction for three neighboring values of return-shock Mach number. The light ion mass fraction for these experiments was 0.95, and we take the spherical geometry factor $\varepsilon = 1/2$ as before. For these Mach numbers, the range in increased stagnation radius from barodiffusion of the argon to fuel center is $\cong 1.25 - 1.4\times$. According to radiation–hydrodynamics

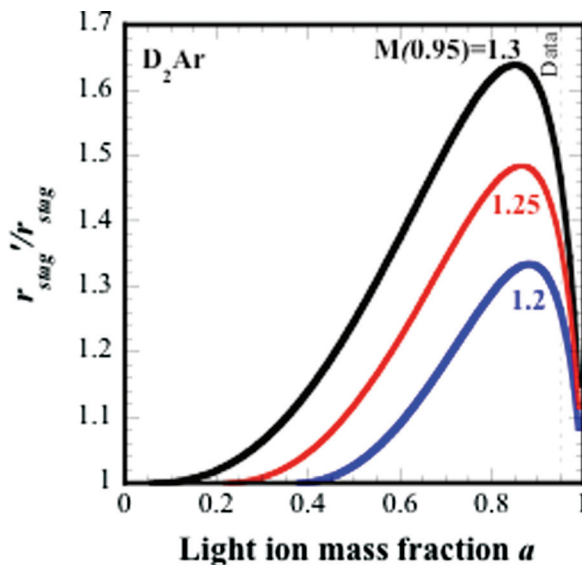


FIG. 7. (Color) Ratio of fuel stagnation radius with and without barodiffusion model vs light ion mass fraction in D₂Ar fuel mixture for three Mach numbers; data shown as dotted line ($\alpha = 0.95$).

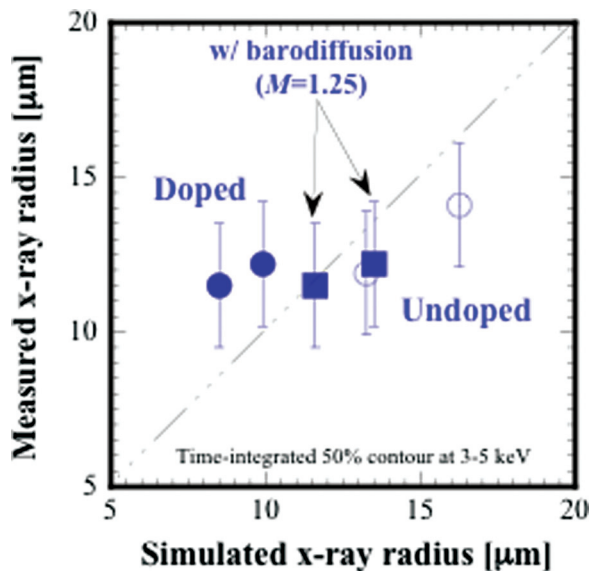


FIG. 8. (Color) Measured time-integrated 50% contour of x-ray self-emission from DD fuel vs simulated x-ray emission for 10 atm DD, indirectly driven implosions of CH capsules doped with 1 at. % Ge with (solid) and without (open) 0.05 atm argon dopant. Solid square points are simulation points adjusted for barodiffusion with Mach number $M = 1.25$.

simulations, the expected ionization state of the argon ions is He-like ($Z_2 \cong 16$). Figure 8 shows the data and simulated x-ray image sizes with and without barodiffusion. Using the barodiffusion model moves the simulations towards much closer agreement with the experimentally inferred image sizes. The migration of the argon ions to fuel center and their associated high emissivity in free-bound radiation could potentially skew the self-emission contours as noted above for D^3He fuel mixtures (Sec. V A). For this case the rate of free-bound radiation $W_{fb} \approx Z^3/(Z+1)^2 T^{5/2} P_d^{3/2} \approx Z^3/(Z+1)^2 P_d^{1/2}$. Taking an upper bound on the argon concentration at fuel center of $8\times$ from spherical convergence, i.e., all of the argon in an annulus of fuel between radii $\Delta_{shock}/2$ and Δ_{shock} migrates to within a sphere of radius $\Delta_{shock}/2$, and a corresponding increase in $\langle Z \rangle = 1.04 \rightarrow 1.31$ from the corresponding higher number fraction of argon ($1-f$), we find an increase in W_{fb} of 10%–25% from barodiffusion. The associated change in the $1/e$ contour of a Gaussian radial self-emission profile is only 5%–10%, which is still relatively modest.

VI. FUTURE

The implications of the D^3He neutron anomaly on the performance of thermonuclear fuels for IFE such as DT are potentially far-reaching. If a similar degradation were to occur for hot-spot ignition using DT fuels, the attractiveness of this ignition mode for IFE applications would suffer significantly. Thus, it is important to understand the nature of this neutron anomaly. If the origin of this anomaly is purely fluid-based, then DT and D^3He fuels should behave similarly. Alternatively, if a plasma-based explanation is at hand then the difference in ionization states of the heavier fuel ion may break the degeneracy of these two fuels and lead to dissimilar behavior. The barodiffusion hypothesis has been

advanced to include the effects of electric fields and to lend a plasma physics explanation for the neutron anomaly in D^3He fuels as well as other standard fuel mixtures in the ICF database.

The barodiffusion explanation for neutron yield and x-ray self-emission image-size anomalies is consistent with experimental trends seen in sub-ignition experiments. For ignition-scale experiments, the main fuel should be largely immune to shock-driven barodiffusive effects, but the earlier mentioned large gradient-scale length version [case (i) in Sec. II] could play some role as in the case of 3He buildup in the DT fuel, for example. The barodiffusion model is largely parameter free, with perhaps only the return-shock Mach number serving as a free parameter operationally, owing to the large spatial gradients and fast time dependence of the fuel dynamics just following shock rebound at the center of the fuel. Further experimental testing of the model is needed. The use of hydrodynamically equivalent DT fuel mixtures would serve as a straightforward test of the model and have key implications for IFE applications. Another experimental test would be the use of (DH) fuels where the model would predict an anomalous increase in neutron production in an equimolar mixture on account of the now heavier deuterium ions barodiffusing toward fuel center.

An ongoing controversy in the performance of fuel mixtures is whether an anomalous (near factor-of-2) deficit of neutron production from “shock flash” or initial shock convergence at fuel center (in contrast to the neutrons produced near peak compression as emphasized herein) is real or not. Experiments reported by Rygg *et al.* using plastic capsules in direct drive show such a deficit,³ whereas Herrmann *et al.* claim no such anomaly with glass shells.⁵ Whether barodiffusion plays a role in this effect or not depends sensitively on the properties of the converging shock leading to shock flash. If the shock front is broadening significantly just before shock flash, the lighter ions may physically cross the origin ahead of the shock and significantly deplete the center of thermonuclear fuel. A resolution of this issue is tailor-made for LSP in a converging geometry where the “macro-particles” can be directly tracked to assess the strength of barodiffusion.

Ultimately, LSP should afford the capability of directly testing the barodiffusion hypothesis by tracking the diffusion of several ion species in the vicinity of a rebounding shock front. A key question to address is whether the ion (spatial) distributions initialized by barodiffusive effects are well maintained up to the time of (compressional) thermonuclear burn.

A growing database on the National Ignition Facility offers further opportunities for testing the barodiffusion hypothesis. Deuterium fuels significantly diluted with 3He and 4He to reduce the neutron fluence on various (unshielded) diagnostics were fielded and lend a potential test of the strength of barodiffusive effects, provided the competing effects of hydrodynamic mix and shock mistiming can be mostly separated. An upcoming ignition tuning campaign using tertiary hydrogen isotopic fuel mixtures may also show some effects of fractionation from barodiffusion. Previous work has shown this to be a modest effect at most,⁷ particularly when the hot-spot fuel mass is dominated by the solid

DT portion of the fuel which is arguably immune to the shock-driven barodiffusion scenario as laid out in this work.

VII. SUMMARY

The recent experimental evidence for strong, self-generated electric fields in imploding ICF targets is inspiring increased interest in understanding the implications of associated plasma physics phenomena beyond the standard, Euler-based fluid descriptions of capsule behavior. At the same time, the ICF database is replete with an assortment of anomalous behaviors that have defied an explanation, particularly for thermonuclear fuel mixtures. These anomalies fall into two principal classes: unexplained neutron yield degradation and core image-size enhancement. The question that we address in this article is whether these anomalies can be explained by multispecies effects such as barodiffusion.

Barodiffusion is a well-known phenomenon in gas dynamics, but its role in ICF has not been studied or acknowledged to date. Our first goal in this work was to redress this omission, and the second to modify the theory of barodiffusion to include various plasma physics phenomena, such as self-generated electric fields and ion charge states. The analysis is found to describe two regimes of interest in ICF: a long scale-length, isothermal, accelerating atmosphere as germane to an imploding capsule, and a short scale-length regime appropriate to a shock front. Our emphasis here has been on the latter case since shock phenomena play a critical role in ICF target performance.

The physical picture of a potential barodiffusive role in ICF target performance is a species separation across a return shock front driven by pressure gradients. The return shock in an ICF implosion has a necessarily low Mach number and an associated large front thickness that enables a substantial volume for diffusion to occur, particularly in a divergent spherical capsule geometry. The episode following shock reversal at fuel center is characterized by large ion mean-free-paths that may promote a redistribution of each ion species. Shortly thereafter, the fuel cools and is compressed, effectively and presumptively locking in the spatial distribution of ions. The lighter ion species barodiffuses towards the front of the shock front, while mass flux conservation applied to a shock requires a reverse diffusion of the heavier ion species and its associated higher electron density from the requirement of charge neutrality. The depletion of the lighter ion species, e.g., deuterium, near fuel center is found to lead to reduced neutron production, while the surplus of heavier ion species, e.g., ^3He or trace amounts of argon dopant, is correlated with a higher central pressure near deceleration onset and reduced stagnation pressure and fuel (peak) compression. The model based on shock-front barodiffusion is found to largely match the various datasets.

Further experimental testing and maturation of the multispecies simulation tools are needed to validate the barodiffusion scenario for ICF fuel fractionation. Several ideas for advanced fuel mixtures, e.g., DH and DT, were suggested to more stringently test the theory. The model as outlined and executed here is analytical in nature, leveraging several key assumptions on shock-front morphology and capsule behavior. Further work with the hybrid PIC code LSP is ongoing with the ultimate goal of tracking the various ion populations versus time in a spherical, converging geometry.

ACKNOWLEDGMENTS

Useful discussions with Warren Garbett, Hans Herrmann, Nels Hoffman, and Riccardo Betti are gratefully acknowledged. This work was performed under the auspices of the Lawrence Livermore National Security, LLC (LLNS) under Contract DE-AC52-07NA27344 and supported by LDRD-08-ERD-062.

- ¹J. R. Rygg, F. H. Séguin, C. K. Li, J. A. Frenje, M. J.-E. Manuel, R. D. Petrasso, R. Betti, J. A. Delettrez, O. V. Gotchev, J. P. Knauer, D. D. Meyerhofer, F. J. Marshall, C. Stoeckl, and W. Theobald, *Science* **319**, 1223 (2008); C. K. Li, F. H. Séguin, J. R. Rygg, J. A. Frenje, M. Manuel, R. D. Petrasso, R. Betti, J. Delettrez, J. P. Knauer, F. Marshall, D. D. Meyerhofer, D. Shvarts, V. A. Smalyuk, C. Stoeckl, O. L. Landen, R. P. J. Town, C. A. Back and J. D. Kilkenny, *Phys. Rev. Lett.* **100**, 225001 (2008).
- ²P. A. Amendt, J. L. Milovich, S. C. Wilks, C. K. Li, R. D. Petrasso, and F. H. Séguin, *Plasma Phys. Controlled Fusion* **51**, 124048 (2009).
- ³J. R. Rygg, J. A. Frenje, C. K. Li, F. H. Séguin, R. D. Petrasso, J. A. Delettrez, V. Yu Glebov, V. N. Goncharov, D. D. Meyerhofer, S. P. Regan, T. C. Sangster, and C. Stoeckl, *Phys. Plasmas* **13**, 052702 (2006).
- ⁴J. D. Lindl, P. Amendt, R. Berger, S. G. Glendinning, S. H. Glenzer, S. W. Haan, R. L. Kauffman, O. L. Landen, and L. J. Suter, *Phys. Plasmas* **11**, 339 (2004).
- ⁵H. W. Herrmann, J. R. Langenbrunner, J. M. Mack, J. H. Cooley, D. C. Wilson, S. C. Evans, T. J. Sedillo, G. A. Kyrala, S. E. Caldwell, C. S. Young, A. Nobile, J. Wermer, S. Paglieri, A. M. McEvoy, Y. Kim, S. H. Batha, C. J. Horsfield, D. Drew, W. Garbett, M. Rubery, V. Yu. Glebov, S. Roberts, and J. A. Frenje, *Phys. Plasmas* **16**, 056312 (2009).
- ⁶T. R. Boehly, D. L. Brown, R. S. Craxton, R. L. Keck, J. P. Knauer, J. H. Kelly, T. J. Kessler, S. A. Kumpan, S. J. Loucks, S. A. Letzring, F. J. Marshall, R. L. McCrory, S. F. B. Morse, W. Seka, J. M. Soures, and C. P. Verdon, *Opt. Commun.* **133**, 495 (1997).
- ⁷P. Amendt, O. L. Landen, H. F. Robey, C. K. Li, and R. D. Petrasso, *Phys. Rev. Lett.* **105**, 115005 (2010).
- ⁸L. D. Landau and E. M. Lifshitz, *Fluid Mechanics* (Pergamon, Oxford, 1987), p. 232.
- ⁹Ya. B. Zel'dovich, and Yu. P. Raizer, *Physics of Shock Waves and High-Temperature Hydrodynamic Phenomena*, edited by W. D. Hayes and R. F. Probstein (Dover, Mineola, New York, 2002).
- ¹⁰M. Y. Jaffrin and R. F. Probstein, *Phys. Fluids* **7**, 1658 (1964).
- ¹¹M. Casanova, O. Larroche, and J.-P. Matte, *Phys. Rev. Lett.* **67**, 2143 (1991).
- ¹²M. M. Marinak, G. D. Kerbel, N. A. Gentile, O. Jones, D. Munro, S. Polaine, T. R. Dittrich, and S. W. Haan, *Phys. Plasmas* **8**, 2275 (2001).
- ¹³D. R. Welch, D. V. Rose, B. V. Oliver, and R. E. Clark, *Nucl. Instrum. Methods Phys. Res. A* **464**, 134 (2001).
- ¹⁴G. A. Sod, *J. Comput. Phys.* **27**, 1 (1978).